Assessing the simulated soil hydrothermal regime of active layer from Noah-MP LSM v1.1 in the permafrost regions of the Qinghai-Tibet Plateau

Xiangfei Li[1,2,3], Tonghua Wu[1,3,*], Xiaodong Wu[1], Jie Chen[1], Xiaofan Zhu[1], Guojie Hu[1], Ren Li[1], Yongping Qiao[1], Cheng Yang[1,3], Junming Hao[1,3], Jie Ni[1,3], Wensi Ma[1,3]

[1] Cryosphere Research Station on the Qinghai-Tibet Plateau, State Key Laboratory of Cryospheric Science, Northwest Institute of Eco-Environment and Resources, Chinese Academy of Sciences, Lanzhou 730000, China

[2] National Cryosphere Desert Data Center, Northwest Institute of Eco-Environment and Resources, Chinese Academy of Sciences, Lanzhou 730000, China

[3] University of Chinese Academy of Sciences, Beijing 100049, China

Correspondence: Tonghua Wu (thuawu@lzb.ac.cn)

Abstract. Extensive and rigorous model inter-comparison is of great importance before application due to the uncertainties in current land surface models (LSMs). Without considering the uncertainties of forcing data and model parameters, this study designed an ensemble of 55296 experiments to evaluate the Noah land surface model with multi-parameterization (Noah-MP) for snow cover events (SCEs), soil temperature (ST) and soil liquid water (SLW) simulation, and investigated the sensitivity of parameterization schemes at a typical permafrost site on the Qinghai-Tibet Plateau. The results showed that Noah-MP systematically overestimates snow cover, which could be greatly resolved when adopting the sublimation from wind and semi-implicit snow/soil temperature time scheme. As a result of the overestimated snow, Noah-MP generally underestimates ST and ST is mostly influenced by the snow process. Systematic cold bias and large uncertainties of soil temperature remains after eliminating the effects of snow, particularly at the deep layers and during the cold season. The combination of roughness length for heat and under-canopy aerodynamic resistance contributes to resolve the cold bias of soil temperature. In addition, Noah-MP generally underestimates top SLW. The RUN process dominates the SLW simulation in comparison of the very limited impacts of all other physical processes. The analysis of the model structural uncertainties and characteristics of each scheme would be constructive to a better understanding of the land surface processes in the permafrost regions of the QTP and further model improvements towards soil hydrothermal regime modeling using the LSMs.

1 Introduction

The Qinghai-Tibet Plateau (QTP) is underlain by the world's largest high-altitude permafrost covering a contemporary area of 1.06×10^6 km^2 (Zou et al., 2017). Under the background of climate warming and intensifying human activities, soil hydrothermal dynamics in the permafrost regions on the QTP has been widely suffering from soil warming (Wang et al., 2021), soil wetting (Zhao et al., 2019), and changes in soil freeze-thaw cycle (Luo et al., 2020).Such changes have not only induced the reduction of permafrost extent, disappearing of permafrost patches and thickening of active layer (Chen et al., 2020), but also resulted in alterations in hydrological cycles (Zhao et al., 2019; Woo, 2012), changes of ecosystem (Fountain et al., 2012; Yi et al., 2011) and damages to infrastructures (Hjort et al., 2018). Therefore, it is very important to monitor and simulate the soil hydrothermal regime to adapt to the changes taking place.

A number of monitoring sites have been established in the permafrost regions of the QTP (Cao et al., 2019). However, it is inadequate to construct the soil hydrothermal state by considering the spatial variability of the ground thermal regime and an uneven distribution of these observations. In contrast, numerical models are competent alternatives. In recent years, land surface models (LSMs), which describe the exchanges of heat, water, and momentum between the land and atmosphere (Maheu et al., 2018), have received significant improvements in the representation of permafrost and frozen ground processes (Koven et al., 2013; Nicolsky et al., 2007; Melton et al., 2019). LSMs are capable of simulating the transient change of subsurface hydrothermal processes (e.g. soil temperature and moisture) with soil heat conduction (-diffusion) and water movement equations (Daniel et al., 2008). Moreover, they could be integrated with the numerical weather prediction system like WRF (Weather Research and Forecasting), making them as effective tools for comprehensive interactions between climate and permafrost (Nicolsky et al., 2007).

Some LSMs have been evaluated and applied in the permafrost regions of the QTP. Guo and Wang (2013) investigated near-surface permafrost and seasonally frozen

ground states as well as their changes using the Community Land Model, version 4

(CLM4). Hu et al. (2015) applied the coupled heat and mass transfer model to identify

the hydrothermal characteristics of the permafrost active layer in the Qinghai-Tibet

Plateau. Using an augmented Noah LSM, Wu et al. (2018) modeled the extent of

permafrost, active layer thickness, mean annual ground temperature, depth of zero

annual amplitude and ground ice content on the QTP in 2010s. Despite those

achievements based on different models, LSMs are in many aspects insufficient in

permafrost regions. For one thing, large uncertainties still exist in the state-of-the-art

LSMs when simulating the soil hydrothermal regime on the QTP (Chen et al., 2019).

For instance, 19 LSMs in CMIP5 overestimate snow depth over the QTP (Wei and Dong,

2015), which could result in the variations of the soil hydrothermal regime in the aspects

of magnitude and vector (cooling or warming) (Zhang, 2005). Moreover, most of the

existing LSMs are not originally developed for permafrost regions. Many of their soil

processes are designed for shallow soil layers (Westermann et al., 2016), but permafrost

would occur in the deep soil. And the soil column is often considered homogeneous,

which cannot represent the stratified soil common on the QTP (Yang et al., 2005). Given

the numerous LSMs and possible deficiencies, it is necessary to assess the

parameterization schemes for permafrost modeling on the QTP, which is helpful to

identify the influential sub-processes, enhance our understanding of model behavior,

and guide the improvement of model physics (Zhang et al., 2016).

Noah land surface model with multi-parameterization (Noah-MP) provides a

unified framework in which a given physical process can be interpreted using multiple

optional parameterization schemes (Niu et al., 2011). Due to the simplicity in selecting

alternative schemes within one modeling framework, it has been attracting increasing

attention in inter-comparison work among multiple parameterizations at point and

watershed scales (Hong et al., 2014; Zheng et al., 2017; Gan et al., 2019; Zheng et al.,

2019; Chang et al., 2020; You et al., 2020a). For example, Gan et al. (2019) carried out

an ensemble of 288 simulations from multi-parameterization schemes of six physical

processes, assessed the uncertainties of parameterizations in Noah-MP, and further

revealed the best-performing schemes for latent heat, sensible heat and terrestrial water storage simulation over ten watersheds in China. You et al. (2020b) assessed the performance of Noah-MP in simulating snow process at eight sites over distinct snow climates and identified the shared and specific sensitive parameterizations at all sites, finding that sensitive parameterizations contribute most of the uncertainties in the multi-parameterization ensemble simulations. Nevertheless, there is little research on the inter-comparison of soil hydrothermal processes in the permafrost regions. In this study, an ensemble experiment of totally 55296 scheme combinations was conducted at a typical permafrost monitoring site on the QTP. The simulated snow cover events (SCEs), soil temperature (ST) and soil liquid water (SLW) of Noah-MP model was assessed and the sensitivities of parameterization schemes at different depths were further investigated. This study could be expected to present a reference for soil hydrothermal simulation in the permafrost regions on the QTP.

This article is structured as follows: Section 2 introduces the study site, atmospheric forcing data, design of ensemble simulation experiments, and sensitivity analysis methods. Section 3 describes the ensemble simulation results of SCEs, ST and SLW, explores the sensitivity and interactions of parameterization schemes. Section 4 discusses the schemes in each physical process. Section 5 concludes the main findings.

2 Methods and materials

2.1 Site description and observation datasets

Tanggula observation station (TGL) lies in the continuous permafrost regions of Tanggula Mountain, central QTP (33.07° N, 91.93° E, Alt.: 5,100 m a.s.l; Fig. 1). This site a typical permafrost site on the plateau with sub-frigid and semiarid climate (Li et al., 2019), filmy and discontinuous snow cover (Che et al., 2019), sparse grassland (Yao et al., 2011), coarse soil (Wu and Nan, 2016; He et al., 2019), and thick active layer (Luo et al., 2016), which are common features in the permafrost regions of the plateau. According to the observations from 2010–2011, the annual mean air temperature of

TGL site was −4.4 °C. The annual precipitation was 375 mm, and of which 80 % is concentrated between May and September. Alpine steppe with low height is the main land surface, whose coverage range is about 40 % ~ 50 % (Yao et al., 2011). The active layer thickness is about 3.15 m (Hu et al., 2017).

The atmospheric forcing data, including wind speed/direction, air temperature/relative humidity/pressure, downward shortwave/longwave radiation, and precipitation, were used to drive the model. These variables above were measured at a height of 2 m and covered the period from August 10, 2010 to August 10, 2012 (Beijing time) with a temporal resolution of 1 hour. Daily soil temperature and liquid moisture at depths of 5 cm, 25 cm, 70 cm, 140 cm, 220 cm and 300 cm from August 10, 2010 to August 9, 2011 (Beijing time) were utilized to validate the simulation results.
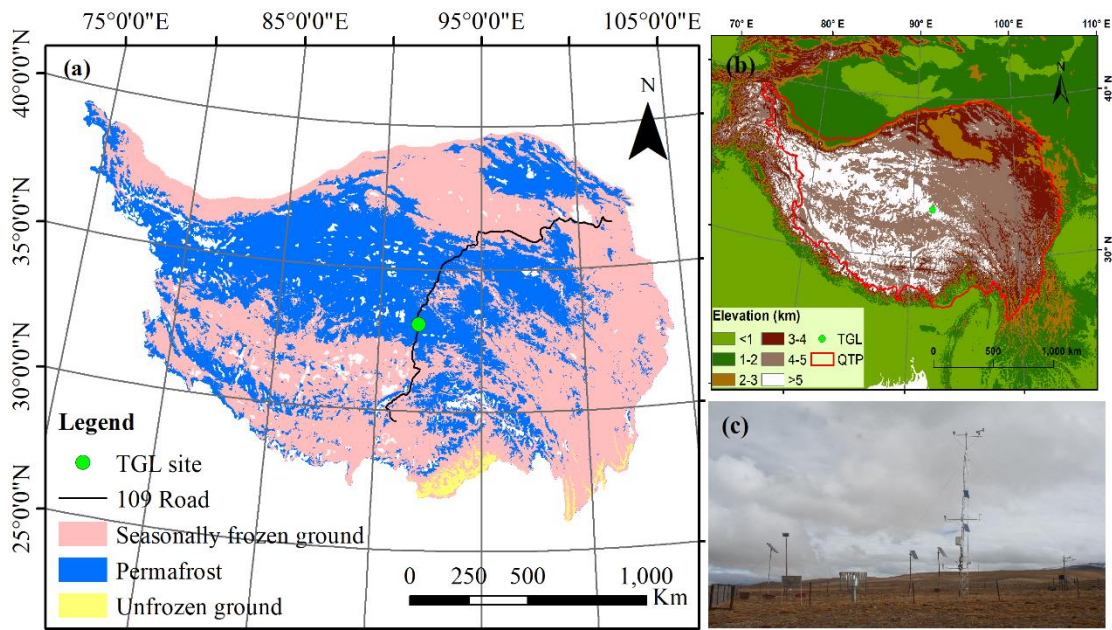
Figure 1. Location and geographic features of study site. (a) Location of observation site and permafrost distribution (Zou et al., 2017). (b) Topography of the Qinghai-Tibet Plateau. (c) Photo of the Tanggula observation station.

2.2 Ensemble experiments of Noah-MP

The offline Noah-MP LSM v1.1 was assessed in this study. The default Noah-MP consists of 12 physical processes that are interpreted by multiple optional

parameterization schemes. These sub-processes include vegetation model (VEG), canopy stomatal resistance (CRS), soil moisture factor for stomatal resistance (BTR), runoff and groundwater (RUN), surface layer drag coefficient (SFC), super-cooled liquid water (FRZ), frozen soil permeability (INF), canopy gap for radiation transfer (RAD), snow surface albedo (ALB), precipitation partition (SNF), lower boundary of soil temperature (TBOT) and snow/soil temperature time scheme (STC) (Table 1). Details about the processes and optional parameterizations can be found in Yang et al. (2011a).

VEG(1) is adopted in the VEG process, in which the vegetation fraction is prescribed according to the NESDIS/NOAA 0.144 degree monthly 5-year climatology green vegetation fraction (https://www.emc.ncep.noaa.gov/mmb/gcip.html), and the monthly leaf area index (LAI) was derived from the Advanced Very High-Resolution Radiometer (AVHRR) (https://www.ncei.noaa.gov/data/, Claverie et al., 2016). Previous studies has confirmed that Noah-MP seriously overestimate the snow events and underestimate soil temperature and moisture on the QTP (Jiang et al., 2020; Li et al., 2020; Wang et al., 2020), which can be greatly resolved by considering the sublimation from wind (Gordon scheme) and a combination of roughness length for heat and under-canopy aerodynamic resistance (Y08-UCT) (Zeng et al., 2005; Yang et al., 2008; Li et al., 2020). For a more comprehensive assessment, we added two physical processes based on the default Noah-MP model, i.e. the snow sublimation from wind (SUB) and the combination scheme process (CMB) (Table 1). In the two processes, users can choose to turn on the Gordon and Y08-UCT scheme (described in the study of Li et al., 2020) or not. As a result, in total 55296 combinations are possible for the 13 processes and orthogonal experiments were carried out to evaluate their performance in soil hydrothermal dynamics.

The Noah-MP model was modified to consider the vertical heterogeneity in the soil profile by setting the corresponding soil parameters for each layer. The soil hydraulic parameters, including the porosity, saturated hydraulic conductivity, hydraulic potential, the Clapp-Hornberger parameter b, field capacity, wilt point, and

saturated soil water diffusivity, were determined using the pedotransfer functions proposed by Hillel (1980), Cosby et al. (1984), and Wetzel and Chang (1987) (Equations S1-S7), in which the sand and clay percentages were based on Hu et al., (2017) (Table S1). In addition, the simulation depth was extended to 8.0 m to cover the active layer thickness of the QTP. The soil column was discretized into 20 layers, whose depths follow the default scheme in CLM 5.0 (Table S1, Lawrence et al., 2018). Due to the inexact match between observed and simulated depths, the simulations at 4 cm, 26 cm, 80 cm, 136 cm, 208 cm and 299 cm were compared with the observations at 5 cm, 25 cm, 70 cm, 140 cm, 220 cm and 300 cm, respectively. A 30-year spin-up was conducted in every simulation to reach equilibrium soil states.

Table 1. The physical processes and options of Noah-MP.

Physical processes	Options
Vegetation model (VEG)	(1) table LAI, prescribed vegetation fraction
	(2) dynamic vegetation
	(3) table LAI, calculated vegetation fraction
	(4) table LAI, prescribed max vegetation fraction
Canopy stomatal resistance (CRS)	(1) Jarvis
	(2) Ball-Berry
Soil moisture factor for stomatal resistance (BTR)	(1) Noah
	(2) CLM
	(3) SSiB
Runoff and groundwater (RUN)	(1) SIMGM with groundwater
	(2) SIMTOP with equilibrium water table
	(3) Noah (free drainage)
	(4) BATS (free drainage)
Surface layer drag coefficient (SFC)	(1) Monin-Obukhov (M-O)
	(2) Chen97
Super-cooled liquid water (FRZ)	(1) generalized freezing-point depression
	(2) Variant freezing-point depression
Frozen soil permeability (INF)	(1) Defined by soil moisture, more permeable
	(2) Defined by liquid water, less permeable
Canopy gap for radiation transfer (RAD)	(1) Gap=F(3D structure, solar zenith angle)
	(2) Gap=zero
	(3) Gap=1-vegetated fraction
Snow surface albedo (ALB)	(1) BATS
	(2) CLASS
Precipitation partition (SNF)	(1) Jordan91
	(2) BATS: $T_{sfc} < T_{frz}+2.2K$
	(3) $T_{sfc} < T_{frz}$

Lower boundary of soil temperature (TBOT)	(1) zero heat flux (2) soil temperature at 8m depth
Snow/soil temperature time scheme (STC)	(1) semi-implicit (2) full implicit
Snow sublimation from wind (SUB)	(1) No (2) Yes
Combination scheme by Li et al.(2020) (CMB)	(1) No (2) Yes

182 BATS (Biosphere–Atmosphere Transfer Model); CLASS (Canadian Land Surface Scheme);

183 SIMGM (Simple topography-based runoff and Groundwater Model); SIMTOP (Simple

184 Topography-based hydrological model); SSiB (Simplified Simple Biosphere model).

185 **2.3 Methods for sensitivity analysis**

186 The simulated snow cover events (SCEs) was quantitatively evaluated using the

187 overall accuracy index (OA) (Toure et al., 2016):

$$OA = \frac{a + d}{a + b + c + d}$$

189 where a is the positive hits, b represents the false alarm, c is the misses, and d

190 represents the negtive hits. The value of OA range from 0 to 1. A higher OA signifies

191 better performance. Ground albedo was used as an indicator for snow events due to a

192 lack of snow depth observations. The days when the daily mean albedo is greater than

193 the observed mean value of the warm and cold season (0.25 and 0.30, respectively) are

194 identified as snow cover.

195 The root mean square error (RMSE) between the simulations and observations

196 were adopted to evaluate the performance of Noah-MP in simulating soil hydrothermal

197 dynamics.

198 To investigate the influence degrees of each physical process on SCEs, ST and

199 SLW, we firstly calculated the mean OA (for SCE) and mean RMSE (for ST and SLW)

200 ($\bar{Y}_j^i$) of the jth parameterization schemes ($j = 1, 2, …$) in the ith process ($i = 1, 2, …$).

201 Then, the maximum difference of $\bar{Y}_j^i$ ($\Delta\overline{OA}$ or $\Delta\overline{RMSE}$) was defined to quantify the

202 sensitivity of the ith process ($i = 1, 2, …$) (Li et al., 2015):

$$\Delta\overline{OA} \ or \ \Delta\overline{RMSE} = \bar{Y}_{max}^i - \bar{Y}_{min}^i$$

204   where $\bar{Y}_{max}^i$ and $\bar{Y}_{min}^i$ are the largest and the smallest $\bar{Y}_j^i$ in the ith process,

205   respectively. For a given physical process, a high $\Delta\overline{OA}$ or $\Delta\overline{RMSE}$ signifies large

206   difference between parameterizations, indicating high sensitiveness of the ith process

207   for SCEs and ST/SLW simulation.

208   The sensitivities of physical processes were determined by quantifying the

209   statistical distinction level of performance between parameterization schemes. The

210   Independent-sample T-test (2-tailed) was adopted to identify whether the distinction

211   level between two schemes is significant, and that between three or more schemes was

212   tested using the Tukey's test. Tukey's test has been widely used for its simple

213   computation and statistical features (Benjamini, 2010). The detailed descriptions about

214   this method can be found in Zhang et al. (2016), Gan et al. (2019), and You et al. (2020a).

215   A process can be considered sensitive when the schemes show significant difference.

216   Moreover, schemes with large mean OA and small mean RMSE were considered

217   favorable for SCEs and ST/SLW simulation, respectively. We distinguished the

218   differences of the parameterization schemes at 95 % confidence level.

219   **3   Results**

220   **3.1 General performance of the ensemble simulation**

221   The performance of Noah-MP for snow simulation was firstly tested by conducting

222   an ensemble of 55296 experiments. Due to a lack of snow depth measurements, ground

223   albedo was used as an indicator for snow cover. Figure 2 shows the monthly variations

224   of observed ground albedo and the simulations produced by the ensemble simulations.

225   The ground albedo was extremely overestimated with large uncertainties when

226   considering the snow options in Noah-MP, indicating the overestimation of snow depth

227   and duration. Such overestimation continued till July.
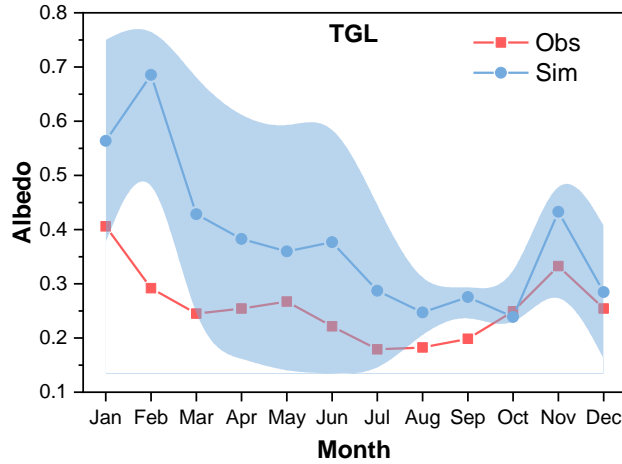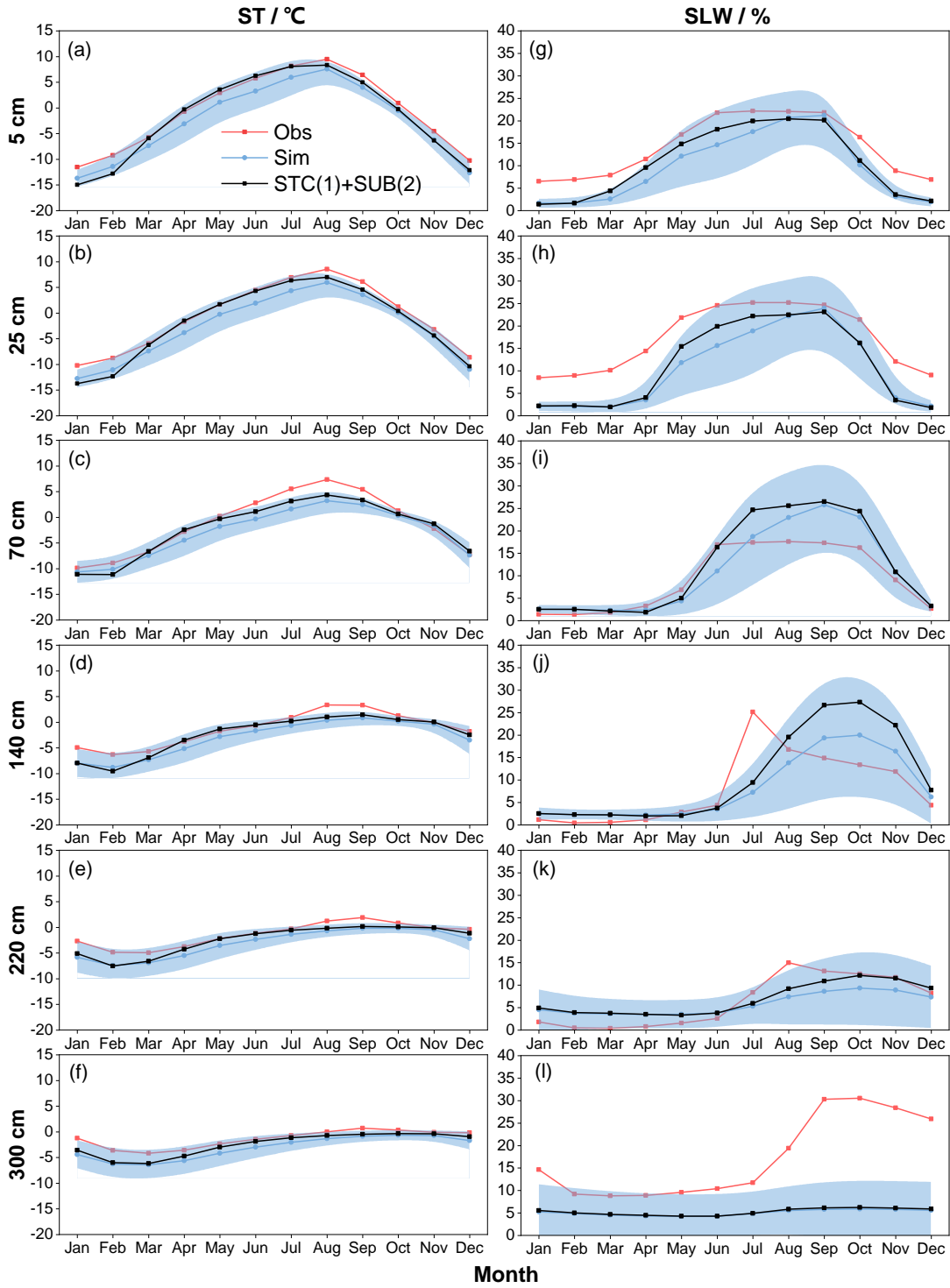
Figure 2. Monthly variations of ground albedo at TGL site for observation (Obs), and the ensemble simulation (Sim). The light blue shadow represents the standard deviation of the ensemble simulation.

Figure 3 illustrates the ensemble simulated and observed annual cycle of ST and SLW at TGL site. The ensemble experiments basically captured the seasonal variability of ST, whose magnitude decreased with soil depth. In addition, the simulated ST in the snow-affected season (October-July) showed relatively wide uncertainty ranges, particularly at the shallow layers. This indicates that the selected schemes perform much differently for snow simulation, resulting in large uncertainties of shallow STs. The simulated ST were generally smaller than the observations with relatively large gaps during the snow-affected season. It indicates that the Noah-MP model generally underestimates the ST, especially during the snow-affected months.

Since the observation equipment can only record the liquid water, soil liquid water (SLW) was evaluated against simulations from the ensemble experiments (Fig. 3). The Noah-MP model generally underestimated surface (5 cm and 25 cm) and deep (220 cm and 300 cm) SLW (Fig. 3g, 3h, 3k, 3l). However, Noah-MP tended to overestimate the SLW at the middle layers of 70 cm and 140 cm. Moreover, the simulated SLW exhibited relatively wide uncertainty ranges, particularly during the warm season (Fig. 3).

Figure 3. Monthly soil temperature (ST in °C) and soil liquid water (SLW in %) at (a, g) 5 cm, (b, h) 25 cm, (c, i) 70 cm, (d, j) 140 cm, (e, k) 220 cm, (f, l) 300 cm at TGL site. The light blue shadow represents the standard deviation of the ensemble simulation. The black line-symbol represents the ensemble mean of simulations with STC(1) and SUB(2).

3.2 Sensitivity of physical processes

3.2.1 Influence degrees of physical processes
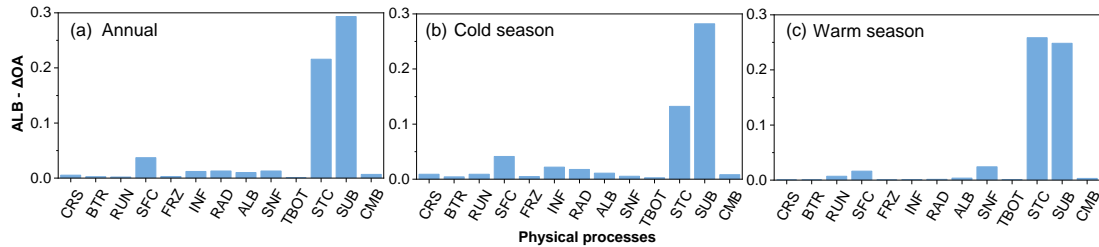
Figure 4. The maximum difference of the mean overall accuracy (OA) for albedo (ALB-ΔOA) in each physical process during the (a) annual, (b) cold season, and (c) warm season at TGL site.

Figure. 4 compares the influence scores of the 13 physical processes based on the maximum difference of the mean OA over 55296 experiments using the same scheme, for SCEs at TGL site. On the whole, the SUB and STC processes had the largest scores for the whole year as well as during both the warm and cold seasons, and the other processes showed a value less than 0.05 (Fig. 4a, 4b, 4c). Moreover, the SUB process had a consistent influence on SCEs while the influence of STC differed with season. In the cold season, the score of SUB process (0.28) was two times more than that of the STC process (Fig. 4b), indicating the relative importance of snow sublimation for SCEs simulation during the cold season. When it comes to the warm season, the influence score of SUB (0.25) did not change much, while that of STC increased to 0.26 and showed a similar influence on SCEs simulation with SUB.
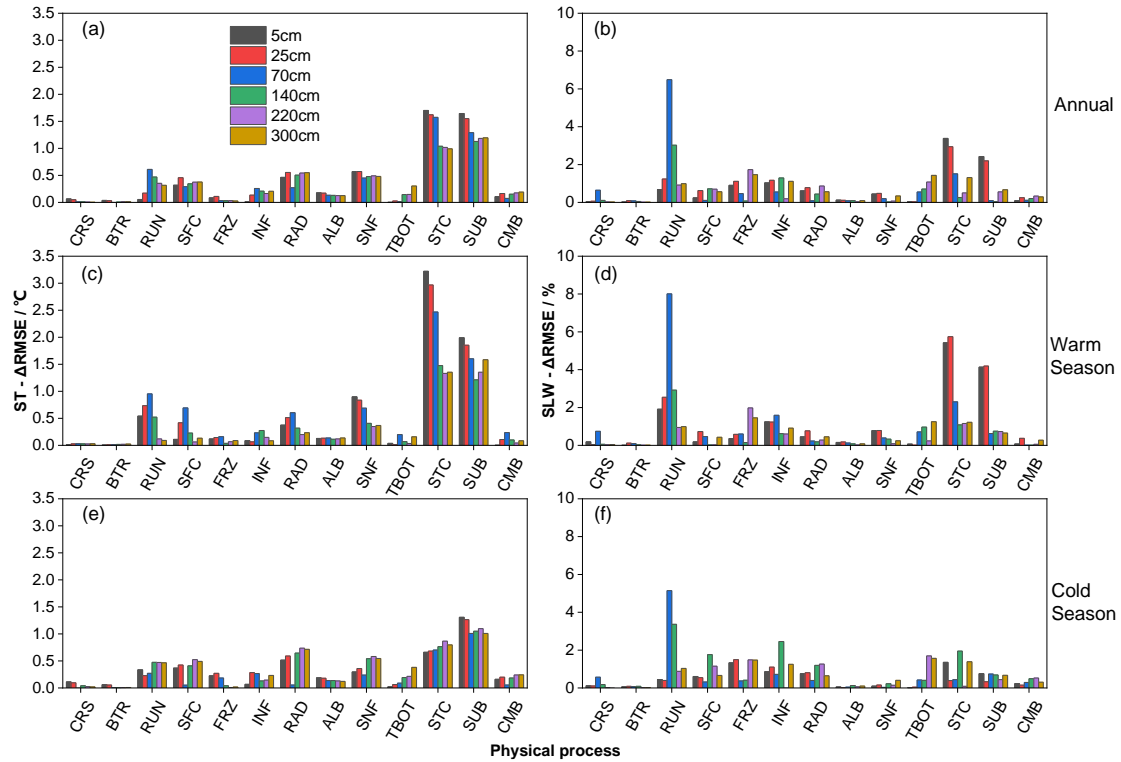
Figure 5. The maximum difference of the mean RMSE for (a, c and e) soil temperature (ST-$\Delta\overline{RMSE}$ in °C) and (b, d and f) soil liquid water (SLW-$\Delta\overline{RMSE}$ in %) in each physical process during the (a and b) annual, (c and d) warm, and (e and f) cold season at different soil depths at TGL site.

Figure. 5 compares the influence scores of the 13 physical processes at different soil depths, based on the maximum difference of the mean RMSE over 55296 experiments using the same scheme, for ST and SLW at TGL site. The snow-related processes, including the STC, SUB and SNF process showed the largest ST-$\Delta\overline{RMSE}$ at all layers, followed by the RAD, SFC and RUN processes. While the ST-$\Delta\overline{RMSE}$ of the other 7 physical processes were less than 0.5°C, among which the influence of CRS and BTR processes were negligible. What's more, the FRZ, INF, and TBOT processes had larger influence scores during the cold season than warm season, and the scores of TBOT were greater in deep soils than shallow soils. During the warm season, the physical processes generally showed more influence on shallow soil temperatures. When it comes to the cold season, the influence of the physical processes on deep layers obviously increased and comparable with that on shallow layers, implying the relatively higher uncertainties of Noah-MP during the cold season.

14

290   Most of the $\Delta\overline{RMSE}$ for SLW are less than 5 %, indicating that all the physical

291   processes have limited influence on the SLW, among which CRS, BTR, ALB, SNF, and

292   CMB showed the smallest effects on SLW (Fig. 5b, 5d, 5f). During the warm season,

293   the RUN process, together with the STC and SUB processes, dominated the

294   performance of SLW simulation, especially at shallow layers (5 cm, 25 cm and 70 cm,

295   Fig. 5d). During the cold season, however, the RUN process dominated the SLW

296   simulation with a great decline of dominance of STC and SUB processes.

297   **3.2.2 Sensitivities of physical processes and general behaviors of**

298   **parameterizations**

299   To further investigate the sensitivity of each process and the general performance

300   of the parameterizations, the Independent-sample T-test (2-tailed) and Tukey's test were

301   conducted to test whether the difference between parameterizations within a physical

302   process is significant (Fig. 6 and 7). In a given sub-process, any two schemes labelled

303   with different letters behave significantly different, and this sub-process therefore can

304   be identified as sensitive. Otherwise, the sub-process is considered insensitive. For

305   simplicity, schemes of insensitive sub-process are not labeled. Moreover, schemes with

306   the letters late in the alphabet have smaller mean RMSEs and outperform the ones with

307   the letters forward in the alphabet. Using the two schemes in CRS process (hereafter

308   CRS(1) and CRS(2)) in Fig. 6 as an example. For the annual and warm season, CRS(1)

309   and CRS(2) were labeled with "B" and "A", respectively. In the cold season, none of

310   them were labeled with letters. As described above, the CRS process was sensitive for

311   SCEs simulation during the annual and warm season, and CRS(1) outperformed

312   CRS(2). However, it was not sensitive during the cold season.

313   Consistent with the influence degrees in Fig. 4, the performance difference

314   between schemes of the STC and SUB for SCEs simulation were significantly greater

315   than other processes. Most other physical processes showed significant but limited

316   difference. Schemes in BTR and TBOT processes, however, had no significant different

317   performance. Specifically, the performance order followed STC(1) > STC(2), SUB(2) >

318   SUB(1), SFC(2) > SFC(1), ALB(2) > ALB(1), CMB(2) > CMB(1) in both annual and

seasonal scales. RAD showed no obvious difference during the warm season, while RAD(3) outperformed RAD(1) and (2) during the cold season. For SNF, SNF(3) generally excel SNF(1) and SNF(2), especially during the warm season.
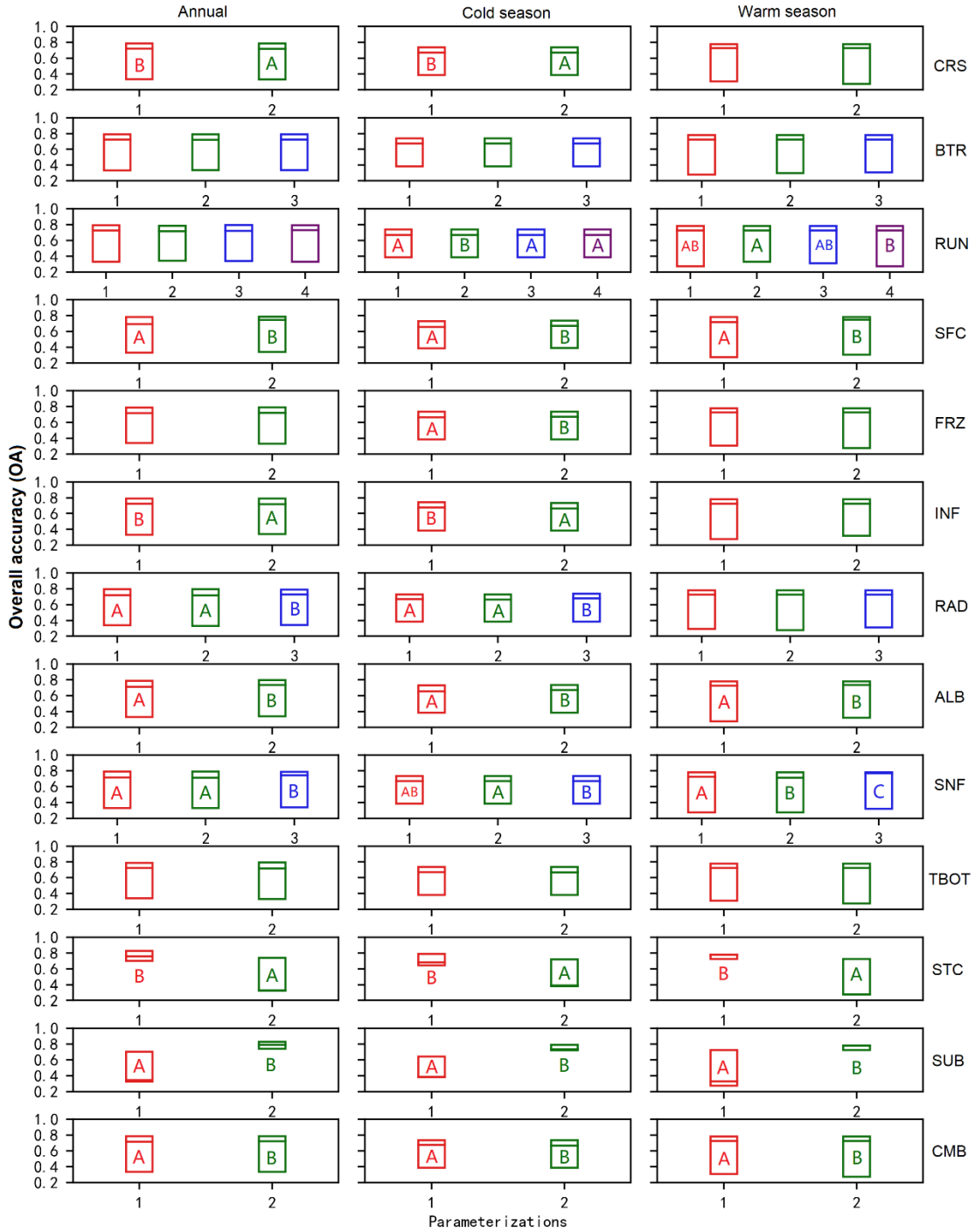
Figure 6. Distinction level for overall accuracy (OA) of snow cover events (SCEs) during the annual, warm, and cold seasons at TGL site. Limits of the boxes represent upper and lower quartiles, lines in the box indicate the median value.

All the physical processes showed sensitivities for ST and SLW simulation in

varying magnitudes except the BTR process and CRS process in most layers. For ST, the performance difference between schemes of the STC, SUB and SNF were obviously greater than other processes, indicating the importance of snow on ST, followed by the RAD, SFC and RUN processes. The performance orders followed STC(1) > STC(2), SUB(2) > SUB(1), SNF(3) > SNF(1) > SNF(2), RAD(3) > RAD(1) > RAD(2), and SFC(2) > SFC(1). For SLW, the RUN, STC, and SUB processes showed significant and higher sensitivities than other physical processes, especially during the warm season and at the shallow layers (Fig. xx). Consistent with that of ST, the performance orders for SLW simulation were STC(1) > STC(2), and SUB(2) > SUB(1).For the RUN process, the performance orders for both ST and SLW simulation generally followed RUN(4) > RUN(1) > RUN(3) > RUN(2) as a whole, among which RUN(1) and RUN(4) presented similar performance during both warm and cold seasons. During both warm and cold seasons, the performance orders for ST simulations were SFC(2) > SFC(1) for SFC process, FRZ(2) > FRZ(1) for FRZ process, and RAD(3) > RAD(1) > RAD(2) for RAD process (Fig. S2 and S3), which are particularly so for SLW simulations at shallow and deep layers.

For ST, both FRZ and INF showed higher sensitivities during the cold season, especially at shallow soils for FRZ and deep soils for INF. FRZ(2)/INF(1) outperformed FRZ(1)/INF(2) for the whole year for ST simulation. Specifically, FRZ(1)/INF(2) performed better at the shallow soils during the warm season while did worse during the cold season compared with FRZ(2)/INF(1). For SLW, FRZ(2)/INF(2) generally preceded FRZ(1)/INF(1) at shallow and deep soils (5 cm, 25 cm, 220 cm, and 300 cm) while did worse at middle soil layers (140 cm and 220 cm).

For ST simulation, the performance sequence in RAD and SNF was RAD(3) > RAD(1) > RAD(2) and SNF(3) > SNF (1) > SNF(2), respectively. For SLW simulation, the sequence become complicated. However, RAD(3) and RAD (3) still outperformed the other two schemes, respectively. ALB(2) was superior to ALB(1) for both ST and SLW simulation. The influence of TBOT on soil hydrothermal arose at deep soils and during cold season, and TBOT(1) excel TBOT (2). CMB(2) outperformed CMB(1) for

ST simulation, so did that for SLW simulation at shallow and deep soils (5 cm, 25 cm, and 300 cm).
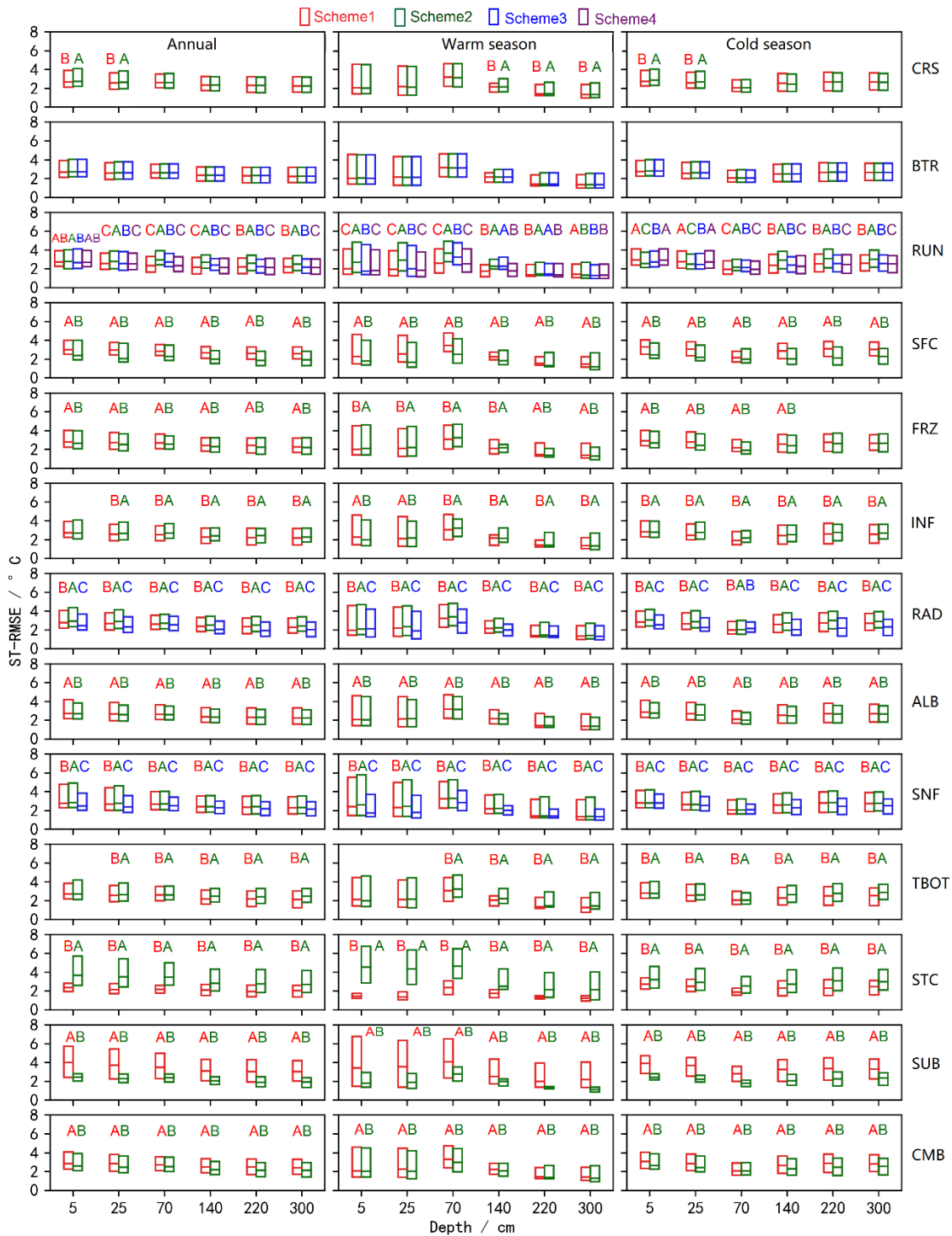
Figure 7. Distinction level for RMSE of ST at different layers during the annual, warm, and cold seasons in the ensemble simulations at TGL site. Limits of the boxes represent upper and lower quartiles, lines in the box indicate the median value.
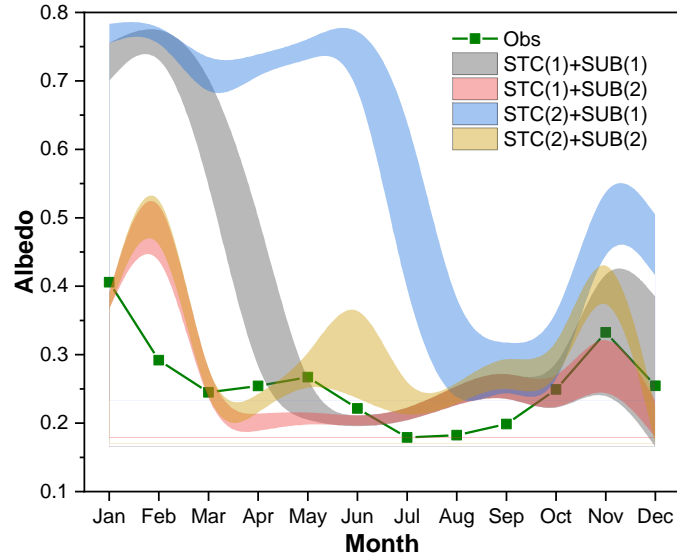
362
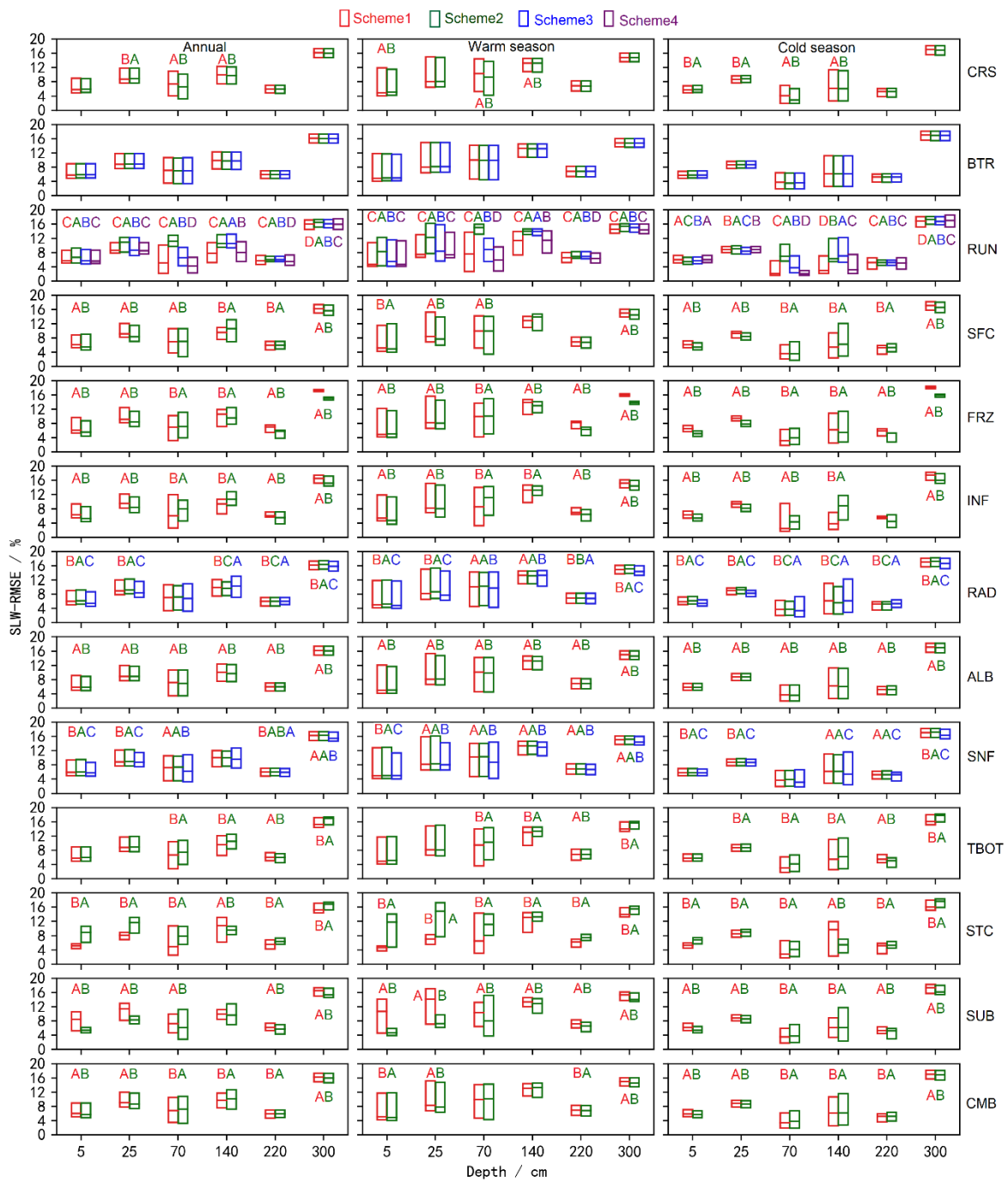
Figure 8. Same as in Figure 7 but for SLW.

## 3.3 Influence of snow cover and surface drag coefficient on soil hydrothermal dynamics

19

Figure 9. Uncertainty interval of ground albedo at TGL site in dominant physical processes (STC and SUB) for snow cover event simulation.

The influence of snow on soil temperature is firstly investigated. The dominant role of STC and SUB in the simulation of SCEs has been identified (Fig. 4 and 6). Interactions between the two physical processes are further analyzed here. Figure 9 compares the uncertainly intervals of the two physics. The duration of snow cover is the longest when STC(2)+SUB(1), followed when STC(2)+SUB(1). Simulations considering SUB(2) generally has a short snow duration. Among the four combinations, STC(1)+SUB(2) is in best agreement with the measurements.

Given the good performance of STC(1)+SUB(2) in simulating SCEs, the influence of snow on soil hydrothermal dynamics is investigated by comparing the total ensemble mean ST and SLW with those adopting STC(1)+SUB(2) (Fig. 3). It can be seen that the ensemble mean ST of simulations adopting STC(1) and SUB(2) are generally higher than the total ensemble means, especially during the spring and summer (Mar.-Aug.). In January and February at shallow layers (5 cm, 25 cm and 70 cm), STC(1)+SUB(2) had a lower ST and showed an insulation effect on ST during the two months. As a whole, however, snow cover has a cooling effect on ST. In addition, along with the improved SCEs and elevated ST, STC(1)+SUB(2) induced moister soil with higher SLW (Fig. 3).
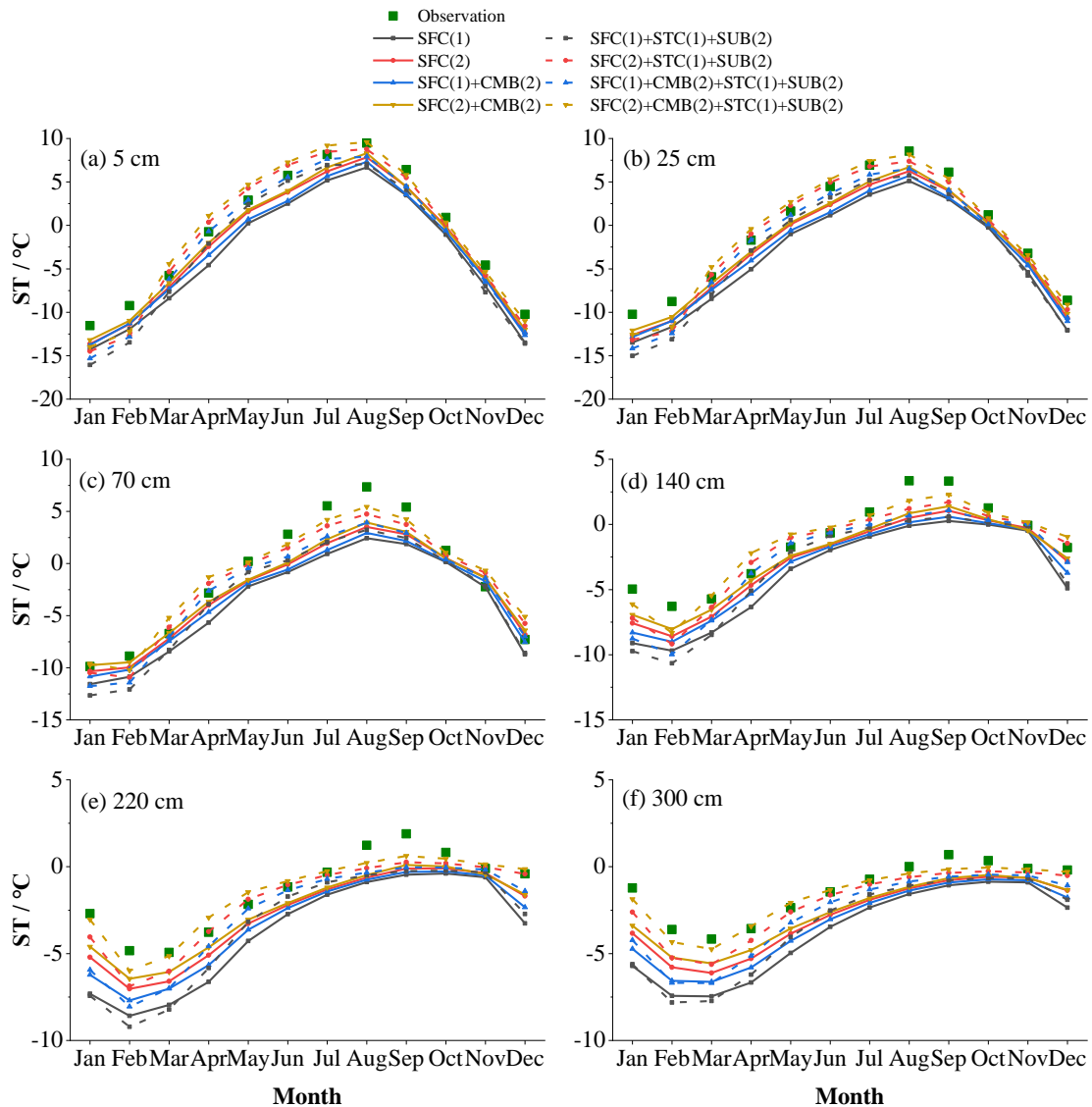
Figure 10. Monthly soil temperature (ST in °C) at (a) 5 cm, (b) 25 cm, (c) 70 cm, (d) 140 cm, (e) 220 cm, (f) 300 cm for the SFC process that consider the CMB(2) and STC(1)+SUB(2) processes or not.

SFC and CMB process using different ways to calculate the surface drag coefficient, which is of great influence for surface energy partitioning and thus ST and SLW. The influence of surface drag coefficient is assessed by comparing the soil temperature before and after considering the combined scheme (CMB(2)) and the effect of snow (STC(1)+SUB(2)) (Fig. 10). SFC(2) tended to produce higher ST than SFC(1), especially during the warming period (January-August). When adopting the combined scheme of Y08 and UCT (CMB(2)), the cold bias were significantly resolved. The

401 performance order followed SFC(2)+CMB(2) > SFC(2) > SFC(1)+CMB(2) > SFC(1).

402 However, considerable underestimations of ST still exist at all layers due to the poor

403 representation of snow process. After eliminating the effects of snow (STC(1)+SUB(2),

404 dash lines in Fig. 10), the simulated ST accordingly increased except in January and

405 February. SFC(2) and SFC(2)+CMB(2) overestimated STs from March to July at

406 shallow layers (5 cm and 25 cm), resulting in good agreements of deep STs with

407 observations. In contrast, the simulated STs at shallow layers (5 cm and 25 cm) by

408 SFC(1) and SFC(1)+CMB(2) were basically consistent with observations from March

409 to July. While large cold bias remained at deep layers.

410 4 Discussion

411 4.1 Snow cover on the QTP and its influence on soil hydrothermal regime

412 Snow cover in the permafrost regions of the QTP is thin, patchy, and short-lived

413 (Che et al., 2019), whose influence on soil temperature and permafrost state is usually

414 considered weak (Jin et al., 2008; Zou et al., 2017; Wu et al., 2018; Zhang et al., 2018;

415 Yao et al., 2019). However, our ensemble simulations showed that the surface albedo

416 is extremely overestimated in both magnitude and duration (Fig. 2), implying an

417 extreme overestimation of snow cover, which is consistent with the studies using Noah-

418 MP model (Jiang et al., 2020; Li et al., 2020; Wang et al., 2020) and widely found in

419 other state-of-the-art LSMs (Wei and Dong, 2015) on the QTP.

420 Great efforts to resolve the overestimation of snow cover in LSMs include

421 considering the vegetation effect (Park et al., 2016), the snow cover fraction (Jiang et

422 al., 2020), the blowing snow (Xie et al., 2019), and the fresh snow albedo (Wang et al.

423 2020). Our results illustrated the superiority of considering the snow sublimation from

424 wind (SUB(2)) and using semi-implicit snow/soil temperature time scheme (STC(1))

425 (Fig. 4, 6 and 9) when simulating snow cover on the QTP. It is consistent with previous

426 conclusions that accounting for the loss resulting from wind contributes to improve

427 snow cover days and depth (Yuan et al., 2016), and that STC(1) has a rapid snow

428 ablation than STC(2) (You et al., 2020a).

429   The impacts of snow cover on soil temperature in magnitude and vector (cooling or

430 warming) depend on its timing, duration, and depth (Zhang et al., 2005). In January and

431 February, the ground heat flux mainly goes upward, the warming effect of simulated

432 snow can be related to the overestimated snow depth that prevent heat loss from the

433 ground. During the spring and summer when snow melts, the cooling effects occurs,

434 mainly because considerable energy that used to heat the ground is reflected due to the

435 high albedo of snow. With the improvement of snow (STC(1)+SUB(2)), the originally

436 overestimated snow melts and infiltrated into the soil, resulting in improved SLWs (Fig.

437 3). And higher soil temperature also contributed to the SLWs according to the freezing-

438 point depression equation, in which SLW exponentially increase with soil temperature

439 for a given site (Niu and Yang, 2006).

4.2 Discussions on the sensitivity of physical processes on soil hydrothermal

441   **simulation**

4.2.1 Canopy stomatal resistance (CRS) and soil moisture factor for stomatal

443 **resistance (BTR)**

444   The biophysical process BTR and CRS directly affect the canopy stomatal

445 resistance and thus the plant transpiration (Niu et al., 2011). The transpiration of plants

446 could impact the ST/SLW through its cooling effect (Shen et al., 2015) and the water

447 balance of root zone (Chang et al., 2020). However, the annual transpiration of alpine

448 steppe is weak due to the shallow effective root zone and lower stomatal control in this

449 dry environment (Ma et al., 2015), which may explain the indistinctive or very small

450 difference among the schemes of the BTR and CRS processes for SCEs (Fig. 8), ST

451 (Fig. 7) and SLW (Fig. 8).

4.2.2 Runoff and groundwater (RUN)

453   In the warm season, different SLWs would result in the difference of the surface

454 energy partitioning and thus different soil temperatures. RUN(2) had the worst

455 performance for simulating ST and SLW (Fig. 7 and 8) among the four schemes, likely

456 due to its higher estimation of soil moisture (Fig. S1) and thus greater sensible heat and

457 smaller ST (Gao et al., 2015). Likewise, RUN(4) was on a par with RUN(1) in the

458 simulation of ST at most layers due to the very small difference in SLW of two schemes

459 (Fig. 8 and S1). For the whole soil column, RUN(4) surpassed RUN(1) and RUN(2) for

460 SLW simulation, both of which define surface/subsurface runoff as functions of

461 groundwater table depth (Niu et al., 2005; Niu et al., 2007). This is in keeping with the

462 study of Zheng et al. (2017) that soil water storage-based parameterizations outperform

463 the groundwater table-based parameterizations in simulating the total runoff in a

464 seasonally frozen and high-altitude Tibetan river. Besides, RUN(4) is designed based

465 on the infiltration-excess runoff (Yang and Dickinson, 1996) in spite of the saturation-

466 excess runoff in RUN(1) and RUN(2) (Gan et al., 2019), which is more common in arid

467 and semiarid areas like the permafrost regions of QTP (Pilgrim et al., 1988). In the cold

468 season, much of the liquid water freezes into ice, which would greatly influence the

469 thermal conductivity of frozen soil considering thermal conductivity of ice is nearly

470 four times that of the equivalent liquid water. Therefore, the impact of RUN is important

471 for the soil temperature simulations at both warm and cold seasons (Fig. 5 and 7).

4.2.3 Surface layer drag coefficient (SFC and CMB)

473 SFC defines the calculations of the surface exchange coefficient for heat and water

474 vapor (CH), which greatly impact the energy and water balance and thus the

475 temperature and moisture of soil (Zeng et al., 2012; Zheng et al., 2012). SFC(1) adopts

476 the Monin-Obukhov similarity theory (MOST) with a general form, while the SFC(2)

477 uses the improved MOST modified by Chen et al. (1997). In SFC(1), the roughness

478 length for heat (Z_{0h}) is taken as the same with the roughness length for momentum (Z_{0m},

479 Niu et al., 2011). SFC(2) adopts the Zilitinkevitch approach for $Z_{0,h}$ calculation

480 (Zilitinkevich, 1995). The difference between SFC(1) and SFC(2) has a great impact

481 on the CH value. Several studies have reported that SFC(2) has a better performance

482 for the simulation of sensible and latent heat on the QTP (Zhang et al., 2016; Gan et al.,

483 2019). The results of T-test in this study showed remarkable distinctions between the

two schemes, where SFC(2) was dramatically superior to SFC(1) (Fig. 7 and 8). SFC(2) produces lower CH than SFC(1) (Zhang et al., 2014), resulting in less efficient ventilation and greater heating of the land surface (Yang et al., 2011b), and substantial improvement of the cold bias of Noah-MP in this study (Fig. 7 and 10).

Both SFC(1) and SFC(2) couldn't produce the diurnal variation of $Z_{0,h}$ (Chen et al., 2010). CMB offers a scheme that considered the diurnal variation of $Z_{0,h}$ in bare ground and under-canopy turbulent exchange in sparse vegetated surfaces (Li et al., 2020). Consistent with previous studies in the QTP (Chen et al., 2010; Guo et al., 2011; Zheng et al., 2015; Li et al., 2020), the simulated ST generally followed SFC(2)+CMB(2) > SFC(2) > SFC(1)+CMB(2) > SFC(1) with/without removing the overestimation of snow (Fig. 10), indicating that CMB(2) contributes to resolve the cold bias of LSMs. However, none of the four combinations could well reproduce the shallow and deep STs simultaneously. When the snow is well-simulated, SFC(2)+CMB(2) performed the best at deep layers at the cost of overestimating shallow STs. Meanwhile, SFC(1)+CMB(1) showed the best agreements at shallow layers with considerable cold bias at deep layers, which can be related to the overestimated frozen soil thermal conductivity (Luo et al., 2009; Chen et al., 2012; Li et al., 2019).

4.2.4 Super-cooled liquid water (FRZ) and frozen soil permeability (INF)

FRZ and INF describe the unfrozen water and permeability of frozen soil, and had a larger influence on ST/SLW during the cold season than warm season as expected (Fig. 5). Specifically, FRZ treats liquid water in frozen soil (super-cooled liquid water) using two forms of freezing-point depression equation. FRZ(1) takes a general form (Niu and Yang, 2006), while FRZ(2) exhibits a variant form that considers the increased surface area of icy soil particles (Koren et al., 1999). FRZ(2) generally yields more liquid water in comparison of FRZ(1) (Fig. S2). INF(1) uses soil moisture (Niu and Yang, 2006) while INF(2) employs only the liquid water (Koren et al., 1999) to parameterize soil hydraulic properties. INF(2) generally produces more impermeable frozen soil than INF(1), which is also found in this study (Fig. S3). For the whole year, INF(1) surpassed INF(2) in simulating STs, which may be related to the more realistic

513   SLWs produced by INF(1) for the whole soil column (Fig. S3).

4.2.5 Canopy gap for radiation transfer (RAD)

515   RAD treats the radiation transfer process within the vegetation, and adopts three

516   methods to calculate the canopy gap. RAD(1) defines canopy gap as a function of the

517   3D vegetation structure and the solar zenith angle, RAD(2) employs no gap within

518   canopy, and RAD(3) treat the canopy gap from unity minus the FVEG (Niu and Yang,

519   2004). The RAD(3) scheme penetrates the most solar radiation to the ground, followed

520   by the RAD(1) and RAD(2) schemes. As an alpine grassland, there is a relative low

521   LAI at TGL site, and thus a quite high canopy gap. So, schemes with a larger canopy

522   gap could realistically reflect the environment. Consequently, the performance

523   decreased in the order of RAD(3) > RAD(1) > RAD(2) for ST/SLW simulation.

4.2.6 Snow surface albedo (ALB) and precipitation partition (SNF)

525   The ALB describe two ways for calculating snow surface albedo, in which the

526   ALB(1) and ALB(2) adopt the scheme from BATS and CLASS LSM, respectively.

527   ALB(2) generally produce lower albedo than ALB(1), especially when the ground

528   covered by snow (Fig. S4). As a result, higher net radiation absorbed by the land surface

529   and more heat is available for heating the soil in ALB(2), which is beneficial for

530   counteracting the cooling effect of overestimated snow on ST (Fig. S5). Along with the

531   higher ST, ALB(2) outperformed ALB(1) for SLW simulation, likely due to more snow

532   melt water offset the dry bias in Noah-MP (Fig. S5).

533   The SNF defines the snowfall fraction of precipitation as a function of surface air

534   temperature. SNF(1) is the most complicated of the three schemes, in which the

535   precipitation is considered rain/snow when the surface air temperature is greater/less

536   than or equal to 2.5/0.5 °C, otherwise, it is recognized as sleet. While SNF(2) and

537   SNF(3) simply distinguish rain or snow by judging whether the air temperature is above

538   2.2 °C and 0 °C or not. The significant difference between three schemes for SCEs

539   simulation during the warm season is consistent with the large difference of snowfall

540   fraction in this period (Fig. 6 and S6). SNF(3) is the most rigorous scheme and produce

541   the minimum amount of snow, followed by SNF(1) and SNF(2) with limited difference

542   (Fig. S6). This exactly explains superiority of SNF(3) for ST and SLW simulation (Fig.

543   7 and 8).

544   4.2.7 Lower boundary of soil temperature (TBOT) and snow/soil temperature time

545   scheme (STC)

546   TBOT process adopts two schemes to describe the soil temperature boundary

547   conditions. TBOT (1) assumes zero heat flux at the bottom of the model, while TBOT(2)

548   adopts the soil temperature at the 8 m depth (Yang et al., 2011a). In general, TBOT(1)

549   is expected to accumulate heat in the deep soil and produce higher ST than TBOT(2).

550   In this study, the two assumptions performed significantly different, especially at the

551   deep soils and during the cold season. Although TBOT(2) is more representative of the

552   realistic condition, TBOT(1) surpassed TBOT(2) in this study. It can be related to the

553   overall underestimation of the model, which can be alleviated by TBOT(1) because of

554   heat accumulation (Fig. S7).

555   Two time discretization strategies are implemented in the STC process, where

556   STC(1) adopts the semi-implicit scheme while STC(2) uses the full implicit scheme, to

557   solve the thermal diffusion equation in first soil or snow layers (Yang et al., 2011a).

558   STC(1) and STC(2) are not strictly a physical processes but different upper boundary

559   conditions of soil column (You et al., 2020a). The differences between STC(1) and

560   STC(2) were significant (Fig. 7). The impacts of the two options on ST is remarkable

561   (Fig. 6), particularly in the shallow layers and during the warm season (Fig. 5). In

562   addition, STC(1) outperformed STC(2) in the ensemble simulated ST(Fig. 7), because

563   STC(1) greatly alleviated the cold bias in Noah-MP (Fig. S8) by producing the higher

564   OA of SCEs (Fig. 6)

565   4.3 Perspectives

566   This study analyzed the characteristics and general behaviors of each

567   parameterization scheme of Noah-MP at a typical permafrost site on the QTP, hoping

568   to provide a reference for simulating permafrost state on the QTP. We identified the

569 systematic overestimation of snow cover, cold bias and dry bias in Noah-MP, and

570 discussed the role of snow and surface drag coefficient on soil hydrothermal dynamics.

571 Further tests at another permafrost site (BLH site, 34.82° N, 92.92° E, Alt.: 4,659 m

572 a.s.l) basically showed consistent conclusions with that at TGL site (see Supplementary

573 files for details), indicating that relevant results and methodologies can be practical

574 guidelines for improving the parameterizations of physical processes and testing their

575 uncertainties towards soil hydrothermal modeling in the permafrost regions of the

576 plateau. Although the site we selected may be representative for the typical environment

577 on the plateau, continued investigation with a broad spectrum of climate and

578 environmental conditions is required to make a general conclusion at regional scale.

579 **5 Conclusions**

580 An ensemble simulation using multi-parameterizations was conducted using the

581 Noah-MP model at the TGL site, aiming to present a reference for simulating soil

582 hydrothermal dynamics in the permafrost regions of QTP using LSMs. The model was

583 modified to consider the vertical heterogeneity in the soil and the simulation depth was

584 extended to cover the whole active layer. The ensemble simulation consists of 55296

585 experiments, combining thirteen physical processes (CRS, BTR, RUN, SFC, FRZ, INF,

586 RAD, ALB, SNF, TBOT, STC, SUB, and CMB) each with multiple optional schemes.

587 On this basis, the general performance of Noah-MP was assessed by comparing

588 simulation results with in situ observations, and the sensitivity of snow cover event, soil

589 temperature and moisture at different depths of active layer to parameterization

590 schemes was explored. The main conclusions are as follows:

591 (1) Noah-MP model tends to overestimate snow cover, which is most influenced by the

592   STC and SUB processes. Such overestimation can be greatly resolved by

593   considering the snow sublimation from wind (SUB(2)) and semi-implicit snow/soil

594   temperature time scheme (STC(1)).

595 (2) Soil temperature is largely underestimated by the overestimated snow cover and

596   thus dominated by the STC and SUB processes. Systematic cold bias and large

uncertainties of soil temperature still exist after eliminating the effects of snow, particularly at the deep layers and during the cold season. The combination of Y08 and UCT contributes to resolve the cold bias of soil temperature.

(3) Noah-MP tend to underestimate soil liquid water content. Most physical processes have limited influence on soil liquid water content, among which the RUN process plays a dominant role during the whole year. The STC and SUB process have a considerable influence on topsoil liquid water during the warm season.

Code availability. The original source code of the offline 1D Noah-MP LSM v1.1 is available at

https://ral.ucar.edu/solutions/products/noah-multiparameterization-land-surface-model-noah-mp-lsm (last access: 23 February 2021). The modified Noah-MP with the consideration of vertical heterogeneity in soil profile, snow sublimation from wind and the combination of roughness length for heat and under-canopy aerodynamic resistance can be downloaded at http://doi.org/10.5281/zenodo.4555449.

Data availability. The 1-hourly forcing data, daily soil temperature and liquid water content at the TGL and BLH sites are available at https://doi.org/10.17632/h7hbd69nnr.2. Soil texture data can be obtained at https://doi.org/10.1016/j.catena.2017.04.011 (Hu et al., 2017). The AVHRR LAI data can be downloaded from https://www.ncei.noaa.gov/data/ (Claverie et al., 2016).

Author contributions. TW and XL conceived the idea and designed the model experiments. XL performed the simulations, analyzed the output, and wrote the paper. JC helped to compile the model in a GNU/Linux (CentOS 7.0) environment. XW, XZ, GH, RL contributed to the conduction of the simulation and interpretation of the results. YQ provided the observations of atmospheric forcing and soil temperature. CY and JH helped in downloading and processing the AVHRR LAI data. JN and WM provide guidelines for the visualization. Everyone revised and polished the paper.

References

Benjamini, Y.: Simultaneous and selective inference: Current successes and future challenges, Biometrical J., 52, 708-721, https://doi.org/10.1002/bimj.200900299, 2010.

Cao, B., Zhang, T., Wu, Q., Sheng, Y., Zhao, L., and Zou, D.: Brief communication: Evaluation and inter-comparisons of Qinghai–Tibet Plateau permafrost maps based on a new inventory of field evidence, The Cryosphere, 13, 511-519, https://doi.org/10.5194/tc-13-511-2019, 2019.

Chang, M., Liao, W., Wang, X., Zhang, Q., Chen, W., Wu, Z., and Hu, Z.: An optimal ensemble of the Noah-MP land surface model for simulating surface heat fluxes over a typical subtropical forest in South China, Agric. For. Meteor., 281, 107815, https://doi.org/https://doi.org/10.1016/j.agrformet.2019.107815, 2020.

Che, T., Hao, X., Dai, L., Li, H., Huang, X., and Xiao, L.: Snow cover variation and its impacts over the Qinghai-Tibet Plateau, Bull. Chin. Acad. Sci., 34, 1247-1253, https://doi.org/10.16418/j.issn.1000-3045.2019.11.007, 2019.

Chen, F., Janjić, Z., and Mitchell, K.: Impact of atmospheric surface-layer parameterizations in the new land-surface scheme of the NCEP Mesoscale Eta Model. Boundary-Layer Meteorol. 85, 391-421, https://doi.org/10.1023/A:1000531001463, 1997.

Chen, R., Yang, M., Wang, X., and Wan, G.: Review on simulation of land-surface processes on the Tibetan Plateau, Sci. Cold Arid Reg., 11, 93-115, https://doi.org/10.3724/SP.J.1226.2019.00093, 2019.

Chen, S., Li, X., Wu, T., Xue, K., Luo, D., Wang, X., Wu, Q., Kang, S., Zhou, H., and Wei, D.: Soil thermal regime alteration under experimental warming in permafrost regions of the central Tibetan Plateau, Geoderma, 372, 114397, https://doi.org/https://doi.org/10.1016/j.geoderma.2020.114397, 2020.

Chen, Y., Yang, K., Zhou, D., Qin, J., and Guo, X.: Improving the Noah land surface model in arid regions with an appropriate parameterization of the thermal roughness length, J. Hydrometeor., 11, 995-1006, https://doi.org/10.1175/2010JHM1185.1, 2010.

Chen, Y., Yang, K., Tang, W., Qin, J., and Zhao, L.: Parameterizing soil organic carbon's impacts on soil porosity and thermal parameters for Eastern Tibet grasslands, Sci. Chin. Earth Sci., 55, 1001-1011, https://doi.org/10.1007/s11430-012-4433-0, 2012.

Claverie, M., Matthews, J. L., Vermote, E. F., and Justice, C. O.: A 30+ year AVHRR LAI and FAPAR climate data record: Algorithm description and validation, Remote Sens., 8, 263, https://doi.org/10.3390/rs8030263, 2016.

Cosby, B. J., Hornberger, G. M., Clapp, R. B., and Ginn, T. R.: A statistical exploration of the relationships of soil moisture characteristics to the physical properties of soils, Water Resour. Res., 20, 682-690, https://doi.org/10.1029/WR020i006p00682, 1984.

Daniel, R., Nikolay, S., Bernd, E., Stephan, G., and Sergei, M.: Recent advances in permafrost modelling, Permafr. Periglac. Process., 19, 137-156, https://doi.org/doi:10.1002/ppp.615, 2008.

Fountain, A. G., Campbell, J. L., Schuur, E. A. G., Stammerjohn, S. E., Williams, M. W., and Ducklow, H. W.: The disappearing cryosphere: Impacts and ecosystem responses to rapid cryosphere loss, BioScience, 62, 405-415, https://doi.org/10.1525/bio.2012.62.4.11, 2012.

Gan, Y. J., Liang, X. Z., Duan, Q. Y., Chen, F., Li, J. D., and Zhang, Y.: Assessment and reduction of the physical parameterization uncertainty for Noah-MP land surface model, Water Resour. Res., 55, 5518-5538, https://doi.org/10.1029/2019wr024814, 2019.

Gao, Y., Kai, L., Fei, C., Jiang, Y., and Lu, C.: Assessing and improving Noah-MP land model simulations for the central Tibetan Plateau, J. Geophys. Res.-Atmos., 120, 9258-9278, https://doi.org/10.1002/2015JD023404, 2015.

Guo, D., and Wang, H.: Simulation of permafrost and seasonally frozen ground conditions on the Tibetan Plateau, 1981-2010, J. Geophys. Res.-Atmos., 118, 5216-5230, https://doi.org/10.1002/jgrd.50457, 2013.

Guo, X., Yang, K., Zhao, L., Yang, W., Li, S., Zhu, M., Yao, T., and Chen, Y.: Critical evaluation of scalar roughness length parametrizations over a melting valley glacier, Boundary-Layer Meteorol., 139(2), 307–332, https://doi.org/10.1007/s10546-010-9586-9, 2011.

He, K., Sun, J., and Chen, Q.: Response of climate and soil texture to net primary productivity and precipitation-use efficiency in the Tibetan Plateau, Pratacultural Science, 36, 1053–1065. https://doi.org/10.11829/j.issn.1001-0629.2019-0036, 2019.

Hillel, D.: Applications of Soil Physics, Academic Press, 400 pp., 1980.

Hjort, J., Karjalainen, O., Aalto, J., Westermann, S., Romanovsky, V. E., Nelson, F. E., Etzelmüller, B., and Luoto, M.: Degrading permafrost puts Arctic infrastructure at risk by mid-century, Nat. Commun., 9, 5147, https://doi.org/10.1038/s41467-018-07557-4, 2018.

Hong, S., Yu, X., Park, S. K., Choi, Y. S., and Myoung, B.: Assessing optimal set of implemented physical parameterization schemes in a multi-physics land surface model using genetic algorithm, Geosci. Model Dev., 7, 2517-2529, https://doi.org/10.5194/gmd-7-2517-2014, 2014.

Hu, G., Zhao, L., Li, R., Wu, T., Wu, X., Pang, Q., Xiao, Y., Qiao, Y., and Shi, J.: Modeling hydrothermal transfer processes in permafrost regions of Qinghai-Tibet Plateau in China, Chin. Geograph. Sci., 25, 713-727, https://doi.org/10.1007/s11769-015-0733-6, 2015.

Hu, G., Zhao, L., Wu, X., Li, R., Wu, T., Xie, C., Pang, Q., and Zou, D.: Comparison of the thermal conductivity parameterizations for a freeze-thaw algorithm with a multi-layered soil in permafrost

705   regions, Catena, 156, 244-251, https://doi.org/10.1016/j.catena.2017.04.011, 2017.

706 Jiang, Y., Chen, F., Gao, Y., He, C., Barlage, M., and Huang, W.: Assessment of uncertainty sources
707   in snow cover simulation in the Tibetan Plateau, J. Geophys. Res.-Atmos., 125, e2020JD032674,
708   https://doi.org/10.1029/2020JD032674, 2020.

709 Jin, H., Sun, L., Wang, S., He, R., Lu, L., and Yu, S.: Dual influences of local environmental
710   variables on ground temperatures on the interior-eastern Qinghai-Tibet Plateau (I): vegetation and
711   snow cover. J. Glaciol. Geocryol. 30, 535–545, 2008.

712 Koren, V., Schaake, J., Mitchell, K., Duan, Q. Y., Chen, F., and Baker, J. M.: A parameterization of
713   snowpack and frozen ground intended for NCEP weather and climate models, J. Geophys. Res.-
714   Atmos., 104, 19569-19585, https://doi.org/10.1029/1999JD900232, 1999.

715 Koven, C., Riley, W., and Stern, A.: Analysis of permafrost thermal dynamics and response to
716   climate change in the CMIP5 earth system models, J. Clim., 26, 1877-1900,
717   https://doi.org/10.1175/JCLI-D-12-00228.1, 2013.

718 Lawrence, D., Fisher, R., Koven, C., Oleson, K., Swenson, S., Vertenstein, M.: Technical description
719   of version 5.0 of the Community Land Model (CLM), Boulder, Colorado, 2018.

720 Li, K., Gao, Y., Fei, C., Xu, J., Jiang, Y., Xiao, L., Li, R., and Pan, Y.: Simulation of impact of roots
721   on soil moisture and surface fluxes over central Qinghai − Xizang Plateau. Plateau Meteor., 34,
722   642-652, https://doi.org/10.7522/j.issn.1000-0534.2015.00035, 2015.

723 Li, R., Zhao, L., Wu, T., Wang, Q. X., Ding, Y., Yao, J., Wu, X., Hu, G., Xiao, Y., Du, Y., Zhu, X.,
724   Qin, Y., Shuhua, Y., Bai, R., Erji, D., Liu, G., Zou, D., Yongping, Q., and Shi, J.: Soil thermal
725   conductivity and its influencing factors at the Tanggula permafrost region on the Qinghai–Tibet
726   Plateau, Agric. For. Meteor., 264, 235-246, https://doi.org/10.1016/j.agrformet.2018.10.011,
727   2019.

728 Li, X., Wu, T., Zhu, X., Jiang, Y., Hu, G., Hao, J., Ni, J., Li, R., Qiao, Y., Yang, C., Ma, W., Wen, A.,
729   and Ying, X.: Improving the Noah-MP Model for simulating hydrothermal regime of the active
730   layer in the permafrost regions of the Qinghai-Tibet Plateau, J. Geophys. Res.-Atmos., 125,
731   e2020JD032588, https://doi.org/10.1029/2020JD032588, 2020.

732 Luo, D., Wu, Q., Jin, H., Marchenko, S., Lyu, L., and Gao, S.: Recent changes in the active layer
733   thickness across the northern hemisphere, Environ. Earth Sci., 75, 555.
734   https://doi.org/10.1007/s12665-015-5229-2, 2016.

735 Luo, S., Lyu, S., Zhang, Y., Hu, Z., Ma, Y. M., Li, S. S., and Shang, L.: Soil thermal conductivity
736   parameterization establishment and application in numerical model of central Tibetan Plateau,
737   Chin. J. Geophys., 52, 919-928, https://doi.org/10.3969/j.issn.0001-5733.2009.04.008, 2009.

738 Luo, S., Wang, J., Pomeroy, J. W., and Lyu, S.: Freeze–thaw changes of seasonally frozen ground
739   on the Tibetan Plateau from 1960 to 2014, J. Clim., 33(21), 9427-9446,
740   https://doi.org/10.1175/JCLI-D-19-0923.1, 2020.

741 Ma, N., Zhang, Y., Guo, Y., Gao, H., Zhang, H., and Wang, Y.: Environmental and biophysical
742   controls on the evapotranspiration over the highest alpine steppe, J. Hydrol., 529, 980-992,
743   https://doi.org/https://doi.org/10.1016/j.jhydrol.2015.09.013, 2015.

744 Maheu, A., Anctil, F., Gaborit, É., Fortin, V., Nadeau, D. F., and Therrien, R.: A field evaluation of
745   soil moisture modelling with the Soil, Vegetation, and Snow (SVS) land surface model using
746   evapotranspiration observations as forcing data, J. Hydrol., 558, 532-545,
747   https://doi.org/https://doi.org/10.1016/j.jhydrol.2018.01.065, 2018.

748 Melton, J., Verseghy, D., Sospedra-Alfonso, R., and Gruber, S.: Improving permafrost physics in

the coupled Canadian Land Surface Scheme (v.3.6.2) and Canadian Terrestrial Ecosystem Model (v.2.1) (CLASS-CTEM), Geosci. Model Dev., 12, 4443-4467, https://doi.org/10.5194/gmd-12-4443-2019, 2019.

Nicolsky, D. J., Romanovsky, V. E., Alexeev, V. A., and Lawrence, D. M.: Improved modeling of permafrost dynamics in a GCM land-surface scheme, Geophys. Res. Lett., 34, L08501, https://doi.org/10.1029/2007gl029525, 2007.

Niu, G.-Y., and Yang, Z.-L.: Effects of vegetation canopy processes on snow surface energy and mass balances, J. Geophys. Res.-Atmos., 109, D23111, https://doi.org/10.1029/2004jd004884, 2004.

Niu, G.-Y., and Yang, Z.-L.: Effects of frozen soil on snowmelt runoff and soil water storage at a continental scale, J. Hydrometeor., 7, 937-952, https://doi.org/10.1175/JHM538.1, 2006.

Niu, G.-Y., Yang, Z.-L., Dickinson, R. E., and Gulden, L. E.: A simple TOPMODEL-based runoff parameterization (SIMTOP) for use in global climate models, J. Geophys. Res.-Atmos., 110, D21106, https://doi.org/10.1029/2005jd006111, 2005.

Niu, G.-Y., Yang, Z.-L., Dickinson, R. E., Gulden, L. E., and Su, H.: Development of a simple groundwater model for use in climate models and evaluation with Gravity Recovery and Climate Experiment data, J. Geophys. Res.-Atmos., 112, D07103, https://doi.org/10.1029/2006jd007522, 2007.

Niu, G.-Y., Yang, Z.-L., Mitchell, K. E., Chen, F., Ek, M. B., Barlage, M., Kumar, A., Manning, K., Niyogi, D., and Rosero, E.: The community Noah land surface model with multiparameterization options (Noah-MP): 1. Model description and evaluation with local-scale measurements, J. Geophys. Res.-Atmos., 116, D12109, https://doi.org/10.1029/2010JD015139, 2011.

Park, S., and Park, S.K.: Parameterization of the snow-covered surface albedo in the Noah-MP Version 1.0 by implementing vegetation effects, Geosci. Model Dev. 9, 1073-1085, https://doi.org/10.5194/gmd-9-1073-2016, 2016.

Pilgrim, D. H., Chapman, T. G., and Doran, D. G.: Problems of rainfall-runoff modelling in arid and semiarid regions, Hydrolog. Sci. J., 33, 379-400, https://doi.org/10.1080/02626668809491261, 1988.

Schaake, J. C., Koren, V. I., Duan, Q. Y., Mitchell, K., and Chen, F.: Simple water balance model for estimating runoff at different spatial and temporal scales, J. Geophys. Res.-Atmos., 101, 7461-7475, https://doi.org/10.1029/95jd02892, 1996.

Shen, M., Piao, S., Jeong, S.-J., Zhou, L., Zeng, Z., Ciais, P., Chen, D., Huang, M., Jin, C.-S., Li, L. Z. X., Li, Y., Myneni, R. B., Yang, K., Zhang, G., Zhang, Y., and Yao, T.: Evaporative cooling over the Tibetan Plateau induced by vegetation growth, Proc. Natl. Acad. Sci. U. S. A., 112, 9299-9304, https://doi.org/10.1073/pnas.1504418112, 2015.

Toure, A., Rodell, M., Yang, Z., Beaudoing, H., Kim, E., Zhang, Y., and Kwon, Y.: Evaluation of the snow simulations from the community land model, version 4 (CLM4). J. Hydrometeor., 17, 153–170, https://doi.org/10.1175/JHM-D-14-0165.1, 2016.

Wang, X., Chen, R., Han, C., Yang, Y., Liu, J., Liu, Z., Guo, S., and Song, Y.: Response of shallow soil temperature to climate change on the Qinghai–Tibetan Plateau, Int. J. Climatol., 41, 1-16, https://doi.org/10.1002/joc.6605, 2021.

Wang, W., Yang, K., Zhao, L., Zheng, Z., Lu, H., Mamtimin, A., Ding, B., Li, X., Zhao, L., Li, H., Che, T., and Moore, J. C.: Characterizing surface albedo of shallow fresh snow and its importance for snow ablation on the interior of the Tibetan Plateau, J. Hydrometeor., 21, 815-827,

https://doi.org/10.1175/JHM-D-19-0193.1, 2020.

Wei, Z., and Dong, W.: Assessment of simulations of snow depth in the Qinghai-Tibetan Plateau using CMIP5 multi-models, Arct. Antarct. Alp. Res., 47, 611-525, https://doi.org/10.1657/AAAR0014-050, 2015.

Westermann, S., Langer, M., Boike, J., Heikenfeld, M., Peter, M., Etzelmuller, B., and Krinner, G.: Simulating the thermal regime and thaw processes of ice-rich permafrost ground with the land-surface model CryoGrid 3, Geosci. Model Dev., 9, 523-546, https://doi.org/10.5194/gmd-9-523-2016, 2016.

Wetzel, P., and Chang, J.-T.: Concerning the relationship between evapotranspiration and soil moisture, J. Clim. Appl. Meteorol., 26, 18-27, https://doi.org/10.1175/1520-0450(1987)026<0018:CTRBEA>2.0.CO;2, 1987.

Woo, M. K.: Permafrost Hydrology, Springer, Berlin, Heidelberg, 2012.

Wu, X., and Nan, Z.: A multilayer soil texture dataset for permafrost modeling over Qinghai-Tibetan Plateau. Paper presented at 2016 IEEE International Geoscience and Remote Sensing Symposium (IGARSS), Beijing, China. https://doi.org/10.1109/IGARSS.2016.7730283, 2016.

Wu, X., Nan, Z., Zhao, S., Zhao, L., and Cheng, G.: Spatial modeling of permafrost distribution and properties on the Qinghai-Tibet Plateau, Permafr. Periglac. Process., 29, 86-99, https://doi.org/10.1002/ppp.1971, 2018.

Xie, Z., Hu, Z., Ma, Y., Sun, G., Gu, L., Liu, S., Wang, Y., Zheng, H., and Ma, W.: Modeling blowing snow over the Tibetan Plateau with the community land model: Method and preliminary evaluation, J. Geophys. Res.-Atmos., 124, 9332–9355, https://doi.org/10.1029/2019jd030684, 2019.

Yang, K., Koike, T., Ye, B., and Bastidas, L.: Inverse analysis of the role of soil vertical heterogeneity in controlling surface soil state and energy partition, J. Geophys. Res.-Atmos., 110, D08101, https://doi.org/10.1029/2004jd005500, 2005.

Yang, K., Koike, T., Ishikawa, H., Kim, J., Li, X., Liu, H., Shaomin, L., Ma, Y., and Wang, J.: Turbulent flux transfer over bare-soil surfaces: Characteristics and parameterization, J. Appl. Meteorol. Clim., 47, 276-290, https://doi.org/10.1175/2007JAMC1547.1, 2008.

Yang, Z.-L., and Dickinson, R. E.: Description of the biosphere-atmosphere transfer scheme (BATS) for the soil moisture workshop and evaluation of its performance, Global Planet. Change, 13, 117-134, https://doi.org/10.1016/0921-8181(95)00041-0, 1996.

Yang, Z.-L., Cai, X., Zhang, G., Tavakoly, A., Jin, Q., Meyer, L., and Guan, X.: The Community Noah Land Surface Model with Multi-Parameterization Options (Noah-MP): Technical Description, 2011a.

Yang, Z.-L., Niu, G.-Y., E. Mitchell, K., Chen, F., B. Ek, M., Barlage, M., Longuevergne, L., Manning, K., Niyogi, D., Tewari, M., and Xia, Y.: The community Noah land surface model with multiparameterization options (Noah-MP): 2. Evaluation over global river basins. J. Geophys. Res.-Atmos. 116, D12110, https://doi.org/10.1029/2010JD015140, 2011b.

Yao, C., Lyu, S., Wang, T., Wang, J., and Ma, C.: Analysis on freezing-thawing characteristics of soil in high and low snowfall years in source region of the Yellow River, Plateau Meteor., 38, 474-483, 2019.

Yao, J., Zhao, L., Gu, L., Qiao, Y., and Jiao, K.: The surface energy budget in the permafrost region of the Tibetan Plateau, Atmos. Res., 102, 394-407, https://doi.org/https://doi.org/10.1016/j.atmosres.2011.09.001, 2011.

Yi, S., Zhou, Z., Ren, S., Ming, X., Yu, Q., Shengyun, C., and Baisheng, Y.: Effects of permafrost degradation on alpine grassland in a semi-arid basin on the Qinghai–Tibetan Plateau, Environ. Res. Lett., 6, 045403, https://doi.org/10.1088/1748-9326/6/4/045403, 2011.

You, Y., Huang, C., Gu, J., Li, H., Hao, X., and Hou, J.: Assessing snow simulation performance of typical combination schemes within Noah-MP in northern Xinjiang, China, J. Hydro., 581, 124380, https://doi.org/10.1016/j.jhydrol.2019.124380, 2020a.

You, Y., Huang, C., Yang, Z., Zhang, Y., Bai, Y., and Gu, J.: Assessing Noah-MP parameterization sensitivity and uncertainty interval across snow climates, J. Geophys. Res.-Atmos., 125, e2019JD030417, https://doi.org/10.1029/2019jd030417, 2020b.

Yuan, W., Xu, W., Ma, M., Chen, S., Liu, W., and Cui, L.: Improved snow cover model in terrestrial ecosystem models over the Qinghai–Tibetan Plateau, Agric. For. Meteor., 218-219, 161-170, https://doi.org/10.1016/j.agrformet.2015.12.004, 2016.

Zeng, X., Dicknson, R., Barlage, M., Dai, Y., Wang, G., and Oleson, K.: Treatment of undercanopy turbulence in land models. J. Clim., 18(23), 5086–5094. https://doi.org/10.1175/Jcli3595.1, 2005.

Zeng, X., Wang, Z., and Wang, A.: Surface skin temperature and the interplay between sensible and ground heat fluxes over arid regions, J. Hydrometeor., 13, 1359-1370, https://doi.org/10.1175/JHM-D-11-0117.1, 2012.

Zhang, G., Chen, F., and Gan, Y.: Assessing uncertainties in the Noah-MP ensemble simulations of a cropland site during the Tibet Joint International Cooperation program field campaign, J. Geophys. Res.-Atmos., 121, 9576-9596, https://doi.org/10.1002/2016jd024928, 2016.

Zhang, H., Su. Y., Jiang, H., Chao, H., and Su, W.: Influence of snow subliming process on land-atmosphere interaction at alpine wetland, J. Glaci. Geocry., 40, 1223-1230, 2018.

Zhang, T.: Influence of the seasonal snow cover on the ground thermal regime: An overview, Reviews of Geophysics, 43, RG4002, https://doi.org/10.1029/2004RG000157, 2005.

Zhao, L., Hu, G., Zou, D., Wu, X., Ma, L., Sun, Z., Yuan, L., Zhou, H., and Liu, S.: Permafrost changes and its effects on hydrological processes on Qinghai-Tibet Plateau, Bull. Chin. Acad. Sci., 34, 1233-1246, https://doi.org/10.16418/j.issn.1000-3045.2019.11.006, 2019.

Zheng, D., van der Velde, R., Su, Z., Wen, J., Booij, M., Hoekstra, A., and Wang, X.: Under-canopy turbulence and root water uptake of a Tibetan meadow ecosystem modeled by Noah-MP, Water Resour. Res., 51, 5735–5755. https://doi.org/10.1002/2015WR017115, 2015.

Zheng, D., van der Velde, R., Su, Z., Wen, J., and Wang, X.: Assessment of Noah land surface model with various runoff parameterizations over a Tibetan river, J. Geophys. Res.-Atmos., 122, 1488-1504, https://doi.org/10.1002/2016jd025572, 2017.

Zheng, H., Yang, Z.-L., Lin, P., Wei, J., Wu, W.-Y., Li, L., Zhao, L., and Wang, S.: On the sensitivity of the precipitation partitioning into evapotranspiration and runoff in land surface parameterizations, Water Resour. Res., 55, 95-111, https://doi.org/10.1029/2017WR022236, 2019.

Zheng, W., Wei, H., Wang, Z., Zeng, X., Meng, J., Ek, M., Mitchell, K., and Derber, J.: Improvement of daytime land surface skin temperature over arid regions in the NCEP GFS model and its impact on satellite data assimilation, J. Geophys. Res.-Atmos., 117, D06117, https://doi.org/10.1029/2011jd015901, 2012.

Zilitinkevich, S.: Non-local turbulent transport pollution dispersion aspects of coherent structure of convective flows, Air Pollution III, Air pollution theory and simulation (H Power, N Moussiopoulos, C A Brebbia, eds) Computational Mechanics Publ , Southampton, Boston, 1, 53-

881   60, 1995.

882   Zou, D., Zhao, L., Sheng, Y., Chen, J., Hu, G., Wu, T., Wu, J., Xie, C., Wu, X., Pang, Q., Wang, W.,

883   Du, E., Li, W., Liu, G., Li, J., Qin, Y., Qiao, Y., Wang, Z., Shi, J., and Cheng, G.: A new map of

884   permafrost distribution on the Tibetan Plateau, The Cryosphere, 11, 2527-2542,

885   https://doi.org/10.5194/tc-11-2527-2017, 2017.

886